

SeisMIC - an Open Source Python Toolset to Compute Velocity Changes from Ambient Seismic Noise

Peter Makus  * ^{1,2}, Christoph Sens-Schönfelder  ¹

¹Helmholtz Center, German Research Center for Geosciences GFZ, Potsdam, Germany, ²Institute for Geological Sciences, Freie Universität Berlin, Berlin, Germany

Author contributions: *Conceptualization*: PM, CS. *Methodology*: CS, PM. *Software*: PM, CS. *Formal Analysis*: PM. *Writing - Original draft*: PM. *Writing - Review & Editing*: CS. *Supervision*: CS. *Funding acquisition*: CS.

Abstract We present SeisMIC, a fast, versatile, and adaptable open-source software to estimate seismic velocity changes from ambient seismic noise. SeisMIC includes a broad set of tools and functions to facilitate end-to-end processing of ambient noise data, from data retrieval and raw data analysis via spectrogram computation, over waveform coherence analysis, to post-processing of the final velocity change estimates. A particular highlight of the software is its ability to invert velocity change time series onto a spatial grid, making it possible to create maps of velocity changes. To tackle the challenge of processing large continuous datasets, SeisMIC can exploit multithreading at high efficiency with an about five-time improvement in compute time compared to MSNoise, probably the most widespread ambient noise software. In this manuscript, we provide a short tutorial and tips for users on how to employ SeisMIC most effectively. Extensive and up-to-date documentation is available online. Its broad functionality combined with easy adaptability and high efficiency make SeisMIC a well-suited tool for studies across all scales.

1 Introduction

Over the past twenty years, the analysis of temporal changes in seismic velocity has become a standard tool in seismology. Seismologists exploit records of repeating sources, such as explosives (e.g., Nishimura et al., 2000; Hirose et al., 2017), vibrators (e.g., Clymer and McEvelly, 1981; Ikuta et al., 2002), airguns (e.g., Wegler et al., 2006; Yang et al., 2018), or earthquake doublets (e.g., Poupinet et al., 1984; Sawazaki et al., 2015), to quantify such changes. Commonly, the analysis of delays focuses on the later arriving, multiply scattered wave train - the so-called coda, which samples the medium to a greater spatial extent than the first-arriving energy and is sensitive even to minute velocity changes (dv/v) in the order of per-mills (Snieder et al., 2002). We refer to this technique as coda wave interferometry.

While active source coda wave interferometry accurately resolves dv/v , studies using artificial sources are logistically challenging and expensive. Repeating natural sources, on the other hand, rarely occur in regular patterns,

*Corresponding author: makus@gfz-potsdam.de

allowing only for a coarse temporal resolution of dv/v in seismically active regions. Sens-Schönfelder and Wegler (2006) obtained dv/v by analysing modifications in the correlations of continuous waveforms. Their method, passive image interferometry (PII), relies on the diffusive energy field of the ubiquitous ambient seismic noise (Sens-Schönfelder and Wegler, 2011). PII has successfully been applied to quantify velocity changes, for example due to seasonal meteorological cycles (e.g., Sens-Schönfelder and Wegler, 2006; Wang et al., 2017), earthquake damage (e.g., Brenguier et al., 2008; Minato et al., 2012), volcanic deformation (e.g., Sens-Schönfelder et al., 2014b; Donaldson et al., 2019), groundwater fluctuations (e.g., Clements and Denolle, 2018; Illien et al., 2021; Mao et al., 2022), landslides (e.g., Bièvre et al., 2018), or climate-change-induced thawing (e.g., Mordret et al., 2016; Lindner et al., 2021). This breadth of applications make PII a widely used methodology.

Processing and analysing continuous waveforms comes with multiple challenges due to the large amount of raw and derived data, such as the need for efficient processing and storage strategies (Arrowsmith et al., 2022). Still today, many scientists use simple "home-grown" scripts to produce results for later publication and interpretation. Often, these scripts lack the required efficiency and make reproducing and adapting analyses cumbersome since there are no agreed-upon standardisations. Only a few software solutions exist for ambient noise seismology, perhaps the most popular among these are MSNoise (Lecocq et al., 2014) and NoisePy (Jiang and Denolle, 2020). However, as we will show and discuss here, the existing software still leaves a niche to fill. To fill this gap, we introduce SeisMIC (Seismological Monitoring using Interferometric Concepts) (Makus and Sens-Schönfelder, 2022), a fast, robust, flexible, and easily-adapted Python tool to compute, process, and analyse dv/v .

2 Modular Structure

2.1 Whom is it for? - The Philosophy behind SeisMIC

As outlined above, monitoring surveys are applied to a broad spectrum of research scopes resulting in a high diversity of requirements for research software. With that in mind, we developed SeisMIC to be flexible and adaptable to user needs. As opposed to working with a black box, users work close to the source code, making it easy to develop individualised workflows or even individually use some modules, submodules, or down to single objects or functions of the code. Yet, the software remains a light and fast package, in which we avoid overhead due to non-essential functionality. For example, in contrast to MSNoise, we avoid heavy database management structure for continuous observatory monitoring, resulting in a significantly faster processing (see section 2.3.2) and giving SeisMIC an advantage in the analysis of campaign based data.

Learning to use a new code and even only determining whether a code satisfies one's need is a large time investment. To guarantee a fast start and a steep learning curve, we aligned SeisMIC closely with ObsPy (Beyreuther et al., 2010), with whose syntax almost all seismologists are familiar. In addition, we host tutorials and extensive, regularly-updated documentation at <https://petermakus.github.io/SeisMIC/>. All objects, methods, and functions have documentation strings according to the Sphinx standard.

As developers, we follow the FAIR principles Hong et al. (2022). That is, we make SeisMIC findable, accessible, interoperable, and reusable. SeisMIC is a community code with clearly communicated community standards, and users can discuss or report issues, suggest changes, or submit pull requests via GitHub. We distribute SeisMIC under

68 the European Union Public License 1.2.

69 Lastly, we keep up to high standards regarding functional robustness. We test functional integrity using a combi-
 70 nation of integral and unit tests. To date, SeisMIC has successfully been applied to a broad range of applications, such
 71 as volcanic environments (Makus et al., 2023b,a), lab-scale applications (Asnar et al., 2023), and cryoseismological
 72 analyses (Nanni et al., 2023).

73 **2.2 Implementation**

74 As commonplace in Python, we structure SeisMIC in a modular fashion. We divide the program into clear modules,
 75 which, in turn, are subdivided into submodules. These modules can either be used separately or connected into a
 76 workflow/pipeline, starting from data retrieval and concluding with the computation, plotting, and postprocessing
 77 of dv/v objects. We show a chart with a simplified overview of SeisMIC’s modular structure in Figure 1.

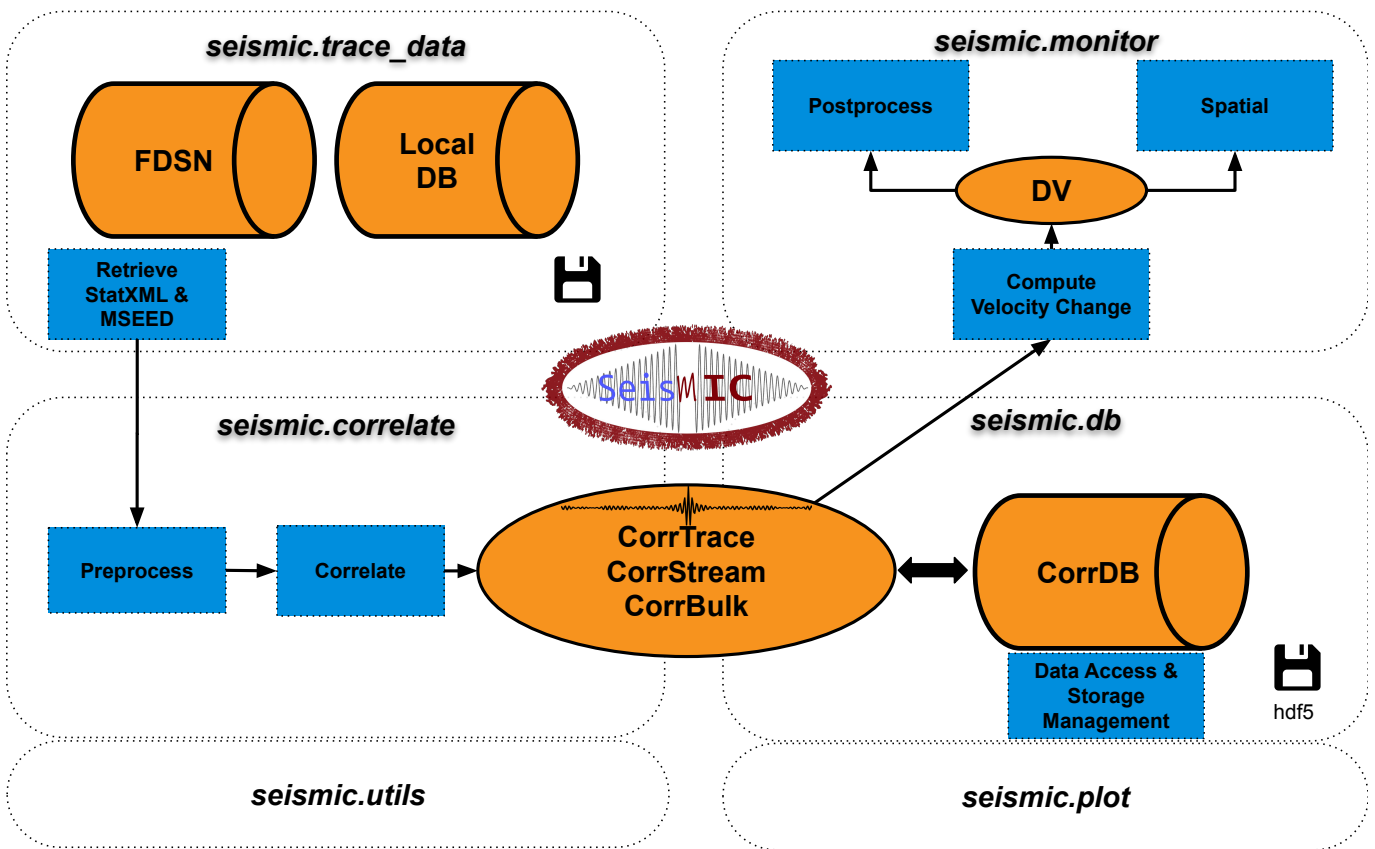


Figure 1 A flowchart summarising SeisMIC’s modules and their purposes. A general workflow starts with data retrieval, continues with the computation of correlation functions, from which a velocity change time series can subsequently be estimated. We illustrate this with the example given in section 3. The depicted floppy disk marks database management modules. Operations and processes are shown in blue, whereas objects and databases are shown in orange. For the sake of simplicity, we omit non-essential objects and functions, instead, the flowchart focuses on the core processes.

78 As shown in Figure 1, SeisMIC consists of four main modules. `seismic.trace_data` hosts the code for reading
 79 raw waveform data and station information. Alternatively, it can request data from FDSN servers. SeisMIC handles
 80 waveform data in *miniseed* format in daily chunks, while it saves station information in *StationXML* format. Generally,
 81 station response information is only necessary if the user should opt to remove the station response before correlat-
 82 ing. However, basic station information, such as the station’s geographic coordinates, is always required.

83 All objects and functions to preprocess waveform data and compute correlation functions (CFs) are located in

84 `seismic.correlate`. We include commonly used preprocessing functions such as detrending, tapering, amplitude
 85 clipping, sign-bit-normalisation, or spectral whitening (Bensen et al., 2007). For a complete and up-to-date list of
 86 preprocessing functions, consult SeisMIC’s documentation. Users can easily import custom processing functions
 87 into the workflow. We compute CFs by transferring traces to matrices, computing the Fourier transform, and then
 88 computing their cross-correlation in the frequency domain. Suppose we want to calculate all available correlations
 89 from a dataset of M waveforms, of which each has N samples. Then, the respective mathematical operations can be
 90 expressed as follows:

91 First, we compute the discrete Fourier transform of the matrix s containing the waveforms in the time domain:

$$92 \quad S_{m,k} = \sum_{n=1}^N s_{m,n} e^{-\frac{i2\pi}{N} kn} \quad (1)$$

93 where i is the imaginary number. Secondly, we obtain the correlation matrix C by computing the product of the
 94 matrix with the complex conjugate of itself. We then repeat the operation M times, each time rolling the complex
 95 conjugate matrix by $j = \{1, 2, \dots, M\}$ lines:

$$96 \quad C_{o,k} = S_{m,k} \overline{S_{m+j,k}} \quad (2)$$

97 where the bar indicates the complex conjugate. In the described scenario, we obtain M^2 CFs, which are subsequently
 98 transferred back to the time domain:

$$99 \quad C_{o,n} = \frac{1}{N} \sum_{k=1}^N C_{o,k} e^{\frac{i2\pi}{N} kn} \quad (3)$$

100 The CFs are then stored as special objects with attributes, plotting and post-processing methods. Finally, SeisMIC
 101 writes the CFs to a storage- and computationally-efficient *HDF5* container (Koranne, 2011).

102 All functionality to estimate velocity changes from the CFs resides in `seismic.monitor`. Currently, SeisMIC sup-
 103 ports the estimation of velocity changes using the stretching technique (Sens-Schönfelder and Wegler, 2006) and we
 104 are implementing the wavelet-cross-spectrum analysis (Mao et al., 2020).

105 The stretching technique compares a reference correlation function \tilde{C}_n to a CF C_n^l computed from data at an
 106 arbitrary subwindow l of the total time series. Note that we omit the index o indicating the station pair since this
 107 operation is independently executed for each station pair. There are several approaches to obtaining \tilde{C} , all with their
 108 unique advantages, SeisMIC supports the use of single or multiple references (Sens-Schönfelder et al., 2014b). In
 109 SeisMIC, we implemented a grid search, in which we evaluate \tilde{C} at a new time vector $\tilde{\tau}$ stretched (or compressed)
 110 with the stretching factor κ_j :

$$111 \quad \tilde{\tau}_j = \tau e^{-\kappa_j} \quad (4)$$

112 Note that we base the exponential stretching on a Taylor extension for small velocity changes. This assumption is
 113 more accurate than the more common $\tilde{\tau}_j \approx \tau(1 + \kappa_j)$ and has the advantage of yielding linearly reversible stretched
 114 functions. In the supplementary material, we provide a derivation.

115 Using our stretched time vector, we obtain a stretched reference correlation matrix with J lines, where J is the

total number of tested stretch factors. Afterwards, we compute the zero-lag correlation (i.e., the normalised dot product) between each stretched reference and C^l :

$$R_j^l = \sum_{n=1}^N \tilde{C}_n^j C_n^l \left(\sum_{n=1}^N (\tilde{C}_n^j)^2 \sum_{n=1}^N (C_n^l)^2 \right)^{-1/2} \quad (5)$$

The stretching factor $\kappa_j = -dv/v$ resulting in the maximum R_j^l corresponds to the negative apparent velocity change at time step l . The maximum value of R measures the velocity change estimate's stability and is often referred to as coherence. We then compute R_j^l for all time steps resulting in the similarity matrix \mathbf{R} , the final velocity change time series, and a corresponding coherence time series. Note that \mathbf{R} is usually not computed for the whole coda, but just for a user-defined subset of lag time samples.

Finally, the computed velocity change time series can be post-processed and plotted using pre-implemented or custom functions. In addition, SeisMIC can invert a set of velocity change time series from different stations onto a map using the inversion method described by [Obermann et al. \(2013a\)](#). To our knowledge, SeisMIC is currently the only software that supports spatial inversion of velocity change time series.

The workflow steps outlined above rely entirely on well-known Python libraries, including *NumPy* ([Harris et al., 2020](#)), *SciPy* ([Virtanen et al., 2020](#)), *ObsPy* ([Beyreuther et al., 2010](#)), *Matplotlib* ([Hunter, 2007](#)), and *h5py* ([Collette et al., 2020](#)). To ensure the best stability, we only utilise the most well-maintained projects and keep the number of dependencies to a minimum. Some of SeisMIC's core functionalities are based on the MIIC software project ([Sens-Schönfelder et al., 2014a](#)). SeisMIC's latest beta version 0.5.3 is compatible with Python 3.10 and 3.11.

2.3 Benchmark and Performance

In ambient noise seismology, it is not uncommon to work with data volumes in the order of terabytes. We address the arising computational and storage challenges with efficient and high-performance computing (HPC) compatible code design enabling parallel computing of correlations, velocity change estimates and spatial inversions, where the computation of CFs is the most expensive operation by a large margin. We implement parallel computing using *mpi4py* ([Dalcin and Fang, 2021](#)), which relies on the message parsing interface (MPI). In contrast to other Python multi-threading solutions, MPI-based solutions work seamlessly on high-performance computing (HPC) and cluster solutions.

2.3.1 Multicore Scaling

To test how SeisMIC's computational performance scales with the number of used threads, we compute autocorrelations from three component data on a single cluster node featuring an Intel Cascadelake CPU structure that is equipped with 2 CPU sockets, each holding 20 physical cores that can each execute two threads in parallel. For our test, we compute CFs from 30 days of waveform data. SeisMIC reads daily chunks of miniseed files, which it subsequently decimates, here to a sampling rate of 25 Hz, after imposing an anti-alias filter. The daily waveforms are then detrended, tapered, and filtered with a pass band between 0.01 and 12 Hz. The data is then sliced into hourly traces, which are again linearly detrended, filtered between 2 and 8 Hz, and clipped if the amplitude exceeds a threshold of 2.5 times its standard deviation. Then, SeisMIC computes hourly CFs in the frequency domain and saves them in a customised HDF5 container after performing an inverse Fourier transform. We provide the *YAML* file containing

151 the processing parameters in the supplementary material. We execute this operation using 1, 2, 4, 8, 16, 32, and 64
 152 threads for data from 1, 2, 4, and 8 stations (i.e., 3, 6, 12, and 24 channels and component combinations). For each
 153 configuration, we repeat the computation ten times.

154 Figure 2 shows the mean processing time and standard deviation over the ten operations per unique $n_{threads}$ -
 155 $n_{stations}$ -combination. We normalise the processing times by the time required for $n_{threads} = 1$ and $n_{stations} = 1$.
 156 While $n_{threads} \leq n_{channels}$, where, in our case, $n_{channels} = 3n_{stations}$, the processing time scales close to linearly with the
 157 number of used threads, indicating an excellent parallel computing performance. As most of the parallel processing
 158 in SeisMIC works on a one-core-per-channel basis, only very little increase can be expected beyond this threshold.
 159 Indeed, for $n_{channels} < n_{threads}$, the code reaches a performance plateau. From here on, the processing time increases
 160 with a further increase of $n_{threads}$, probably due to MPI's communication overhead. Based on the shown results, we
 161 would discourage hyperthreading (i.e., using more threads than available physical cores), which leads to a significant
 162 performance drop. Generally, one should not employ more threads than the total number of available channels for
 163 the computation of correlation functions or the total number of channel combinations for the dv/v estimation.

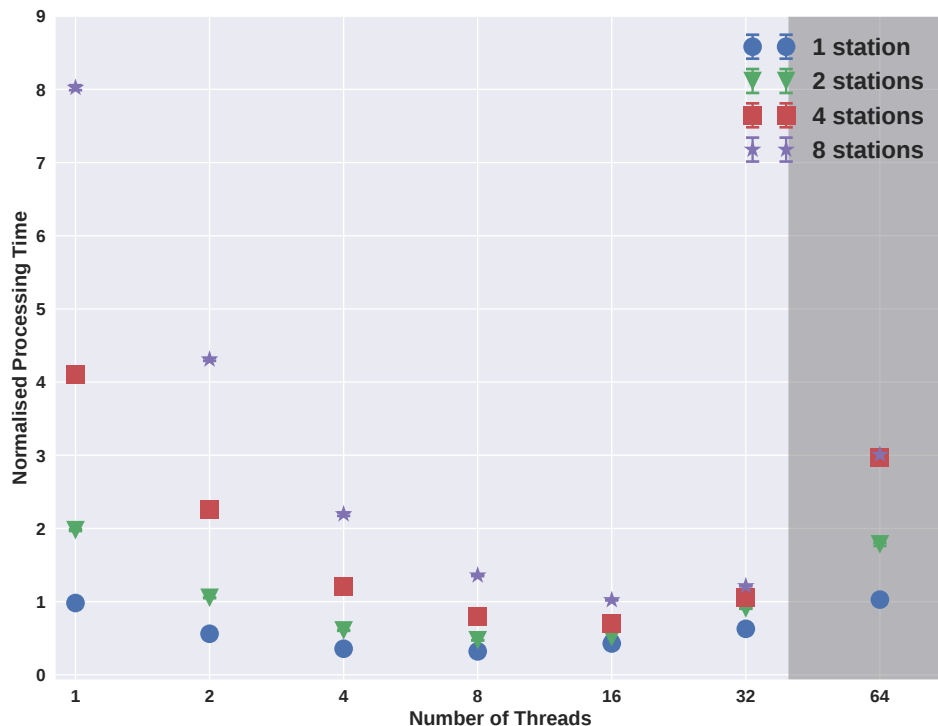


Figure 2 Multi-core scaling properties of SeisMIC. We show compute times for auto-correlations as a function of number of three-component datasets and number of parallel processing threads. The data points correspond to the mean processing time and the error bars to its standard deviation for ten operations (mostly too small to be visible). The processing times are normalised by the time needed to compute the correlations for one station using only one thread. The shaded area marks the area where the number of threads exceeds the number of physical cores, 40, i.e., the area where hyperthreading is employed.

164 2.3.2 Comparison with MSNoise

165 To analyse how SeisMIC's processing speed compares to the latest release of MSNoise (Lecocq et al., 2014), 1.6.3,
 166 we choose to calculate cross-correlations, which is the most expensive operation in a standard workflow, taking up
 167 more than 95% of the total compute time. In this benchmark, we retrieve hourly cross-correlations for 14 days of raw
 168 waveform data between eight 3-component broadband seismometers sampling at 100 Hz. We set the preprocessing

169 to be identical for both programs. First, the data are decimated to 25 Hz. Subsequently, we detrend, taper, and band-
 170 pass filter the data between 2 and 4 Hz. Before computing the CFs, we apply one-bit normalisation and spectral
 171 whitening. Finally, we save the hourly CFs and daily CF stacks for all six unique component combinations with a
 172 length of 50 seconds. We perform the benchmark on the same Intel-Cascadelake-based node that we use in section
 173 [2.3.1](#).

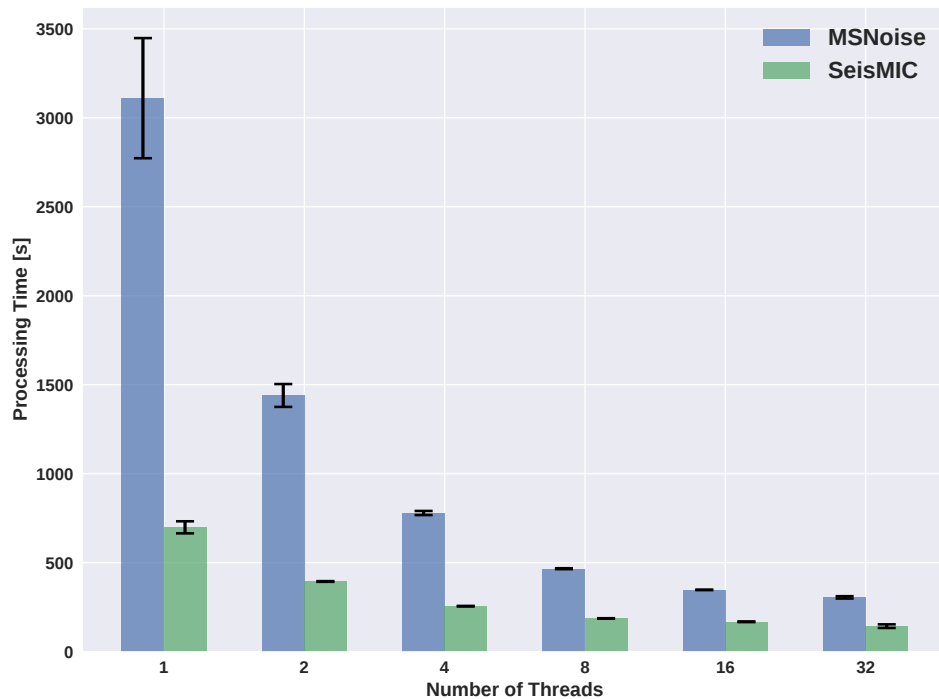


Figure 3 Compute times for a cross-correlation workflow for all six unique component combinations between eight seismic stations using MSNoise 1.6.3 (Lecocq et al., 2014) and SeisMIC 0.5.3. The height of the bars indicates the mean processing time over five iterations with the error bars representing the standard deviation. For hardware information and the exact parametrisation of the workflows, consult the text body.

174 We show the processing times required by MSNoise and SeisMIC for the outlined operation as a function of em-
 175 ployed threads in Figure 3. Despite having received a significant performance boost with the update to version 1.6.x,
 176 MSNoise still needs about five times as long and thrice as much random access memory (RAM) as SeisMIC to execute
 177 the cross-correlation workflow, putting SeisMIC at a similar efficiency level as NoisePy (see Jiang and Denolle, 2020).
 178 In addition, SeisMIC offers a broader range of preprocessing options than NoisePy or MSNoise. MSNoise creates one
 179 miniseed file per CF, resulting in less complex and more evenly distributed writing operations. For this benchmark,
 180 this translates to a slightly better scaling but a high number of files, which can be undesirable for large datasets.
 181 SeisMIC, on the other hand, creates one file per component combination. In every case, MSNoise remains more
 182 than twice as slow as SeisMIC. Note that the shown times do not include the time that MSNoise takes to set up a
 183 database and scan new data, which can take a significant amount of time, whereas these operations are practically
 184 instantaneous in SeisMIC.

185 While the presented results are encouraging, we remark that we could decrease compute times even further
 186 by exploiting the potential of modern graphic processing units (GPUs), which can correlate ambient seismic noise
 187 with high efficiency (Clements and Denolle, 2021; Wu et al., 2022). Implementing such algorithms belongs to the
 188 intermediate-term goals of SeisMIC's development.

3 A Practical Example of a Workflow: From Raw Waveform Data to a Velocity Change Time Series

In this section, we demonstrate how to obtain a dv/v time series using a minimal workflow in SeisMIC. In the supplementary material, we provide two Jupyter notebooks containing the source code used for this workflow. The exemplary data are recorded by station X9.IR1 around the date of the M7.2 Zhupanov earthquake in Kamchatka, Russia. In the following, we investigate the impact of the event on the seismic velocity in the station's vicinity. A discussion of the result lies beyond the scope of this technical paper and has already been performed by [Makus et al. \(2023b\)](#). We conducted this analysis using SeisMIC's implemented workflow, which is parametrised using a simple *YAML* file (see supplementary material). In the following, we will take a step-by-step tour through said workflow and provide some minimal code examples. For further examples, we advise the reader to consult SeisMIC's documentation and our GitHub page.

3.1 Data Retrieval

To start, we download data from an FDSN-compatible server. In our case, we download data from station X9.IR1, available over the GEOFON FDSN service ([Quinteros et al., 2021](#)). For conciseness, we restrict this example to 11 days of data from 25 January to 5 February 2016. This short time window comprises the 28 January Zhupanov earthquake, whose coseismic velocity drop we want to investigate. In SeisMIC, we can initiate the data download using the `Store_Client` class and its method `download_waveforms_md1`:

Listing 1 Downloading data using SeisMIC

```
from obspy import UTCDateTime

from seismic.trace_data.waveform import Store_Client

starttime = UTCDateTime(2016, 1, 25)
endtime = UTCDateTime(2016, 2, 5)

# Decide where data are stored
sc = Store_Client('GEOFON', '/path/to/project', read_only=False)
sc.download_waveforms_md1(
    starttime, endtime, clients=['GEOFON'], network='X9',
    station='IR1', location='*', channel='HHE')
```

Under the hood, this will initiate ObsPy's ([Beyreuther et al., 2010](#)) `MassDownloader` to download continuous waveform data from the specified station if not already present locally. Here, we will compute autocorrelations using only the east component of the seismogram. We can use SeisMIC to get a first idea of the spectral content of our waveform and to investigate in which frequency bands we might find stable noise sources suitable for PII. We show a spectrogram computed using Welch windows (see, e.g., [Barbe et al., 2010](#)) as implemented in SeisMIC in Figure 4.

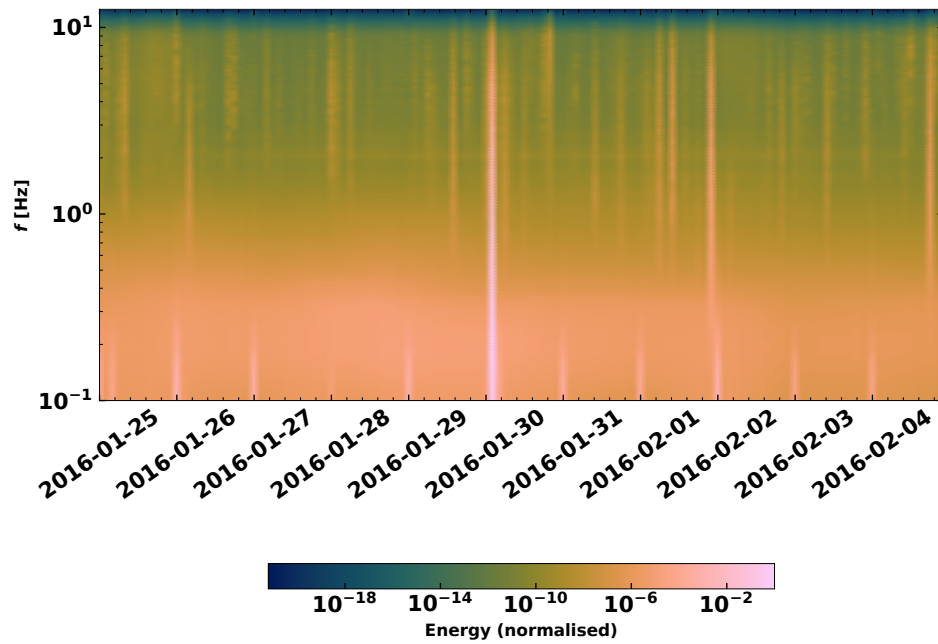


Figure 4 Time dependent spectrogram of the raw waveform at X9.IR1. We compute the spectrogram after removing the instrument response using 2 hours Welch windows. Note the energy spike caused by the Zhupanov earthquake. The energy amplitude is normalised by its maximum.

3.2 Computing Autocorrelations

After downloading the waveforms, we can correlate them to obtain CFs. When computing correlations, we have ample preprocessing options, which, for brevity, we will not discuss here in detail. Most fundamentally, we must set the correlation length (i.e., the duration of the time windows to be correlated), the correlation method (in our case, autocorrelation), and the frequency window to be filtered. The user defines all options in the *YAML* file, but they can also provide parameters in a Python dictionary. For this example, we choose a correlation length of one hour and a frequency band between 2 and 4 Hz. In SeisMIC, the `Correlator` class handles the correlation workflow.

Listing 2 Downloading data using SeisMIC

```

230 from seismic.correlate.correlate import Correlator
231
232 # sc is the previously initiated Store_Client
233 c = Correlator(sc, options='path/to/params.YAML')
234 st = c.pxcorr()

```

To illustrate the syntax of the parameter file, we show an extract of it below. Note that the keys `preProcessing`, `TDpreProcessing`, and `FDpreProcessing` can also import custom, external functions as long as input arguments and return objects follow a predefined syntax.

Listing 3 params.YAML

```

238 ...
239 read_start : '2016-01-25 00:00:01.0'
240 read_end : '2016-02-05 00:00:00.0'
241 sampling_rate : 25
242 remove_response : False

```

```

243 combination_method : 'autoComponents'
244 preProcessing : [
245     {'function':'seismic.correlate.preprocessing_stream.detrend_st',
246      'args':{'type':'linear'}},
247     {'function':'seismic.correlate.preprocessing_stream.cos_taper_st',
248      'args':{'taper_len': 100,
249             'lossless': True}},
250     {'function':'seismic.correlate.preprocessing_stream.stream_filter',
251      'args':{'ftype':'bandpass',
252             'filter_option':{'freqmin':0.01, 'freqmax':12.49}}}]
253 subdivision:
254     corr_inc : 3600
255     corr_len : 3600
256     ...
257 corr_args : {'TDpreProcessing':[
258     {'function':'seismic.correlate.preprocessing_td.detrend',
259      'args':{'type':'linear'}},
260     {'function':'seismic.correlate.preprocessing_td.TDfilter',
261      'args':{'type':'bandpass','freqmin':2,'freqmax':4}},
262     ],
263     'lengthToSave':25,
264     'center_correlation':True,
265     'normalize_correlation':True,
266     ...
267     }
268     ...

```

269 Its `pxcorr` method will internally handle preprocessing and correlation. It will also initiate MPI to enable parallel
270 processing. In Figure 5, we plotted the CFs using SeisMIC's plotting tools. Due to the high noise level in the chosen
271 time window and frequency band, a well-defined coda emerges from the CFs (see Makus et al., 2023b, for details).

272 3.3 Waveform Coherence

273 For a first assessment of which frequency bands are well-suited for a velocity change analysis, we can use a spec-
274 trogram like the one we show in Figure 4. Additionally, one can use SeisMIC's waveform coherence function. The
275 waveform coherence corresponds to the averaged zero-lag cross-correlation between a reference CF and CFs at time
276 t (Steinmann et al., 2021). In Figure 6, we show the waveform coherence for our exemplary dataset computed be-
277 tween hourly CFs and the average CF as a reference. We determine the coherence for 5s long lapse-time windows
278 and one-octave-wide frequency bands jointly for positive (causal) and negative (acausal) lag times. SeisMIC computes
279 waveform coherence using the `Monitor` class and its `compute_waveform_coherence_bulk()` method (see supple-
280 mentary material).

281 Figure 6 leads us to infer a high stability and energy content between 0.5 and 4 Hz. The coherence remains high
282 until late lag times, e.g. for 3 Hz centre frequency, up to 75 periods. From this, we infer a highly scattering medium
283 paired with a high energy content in this frequency band originating from the volcanic system (see Makus et al.,

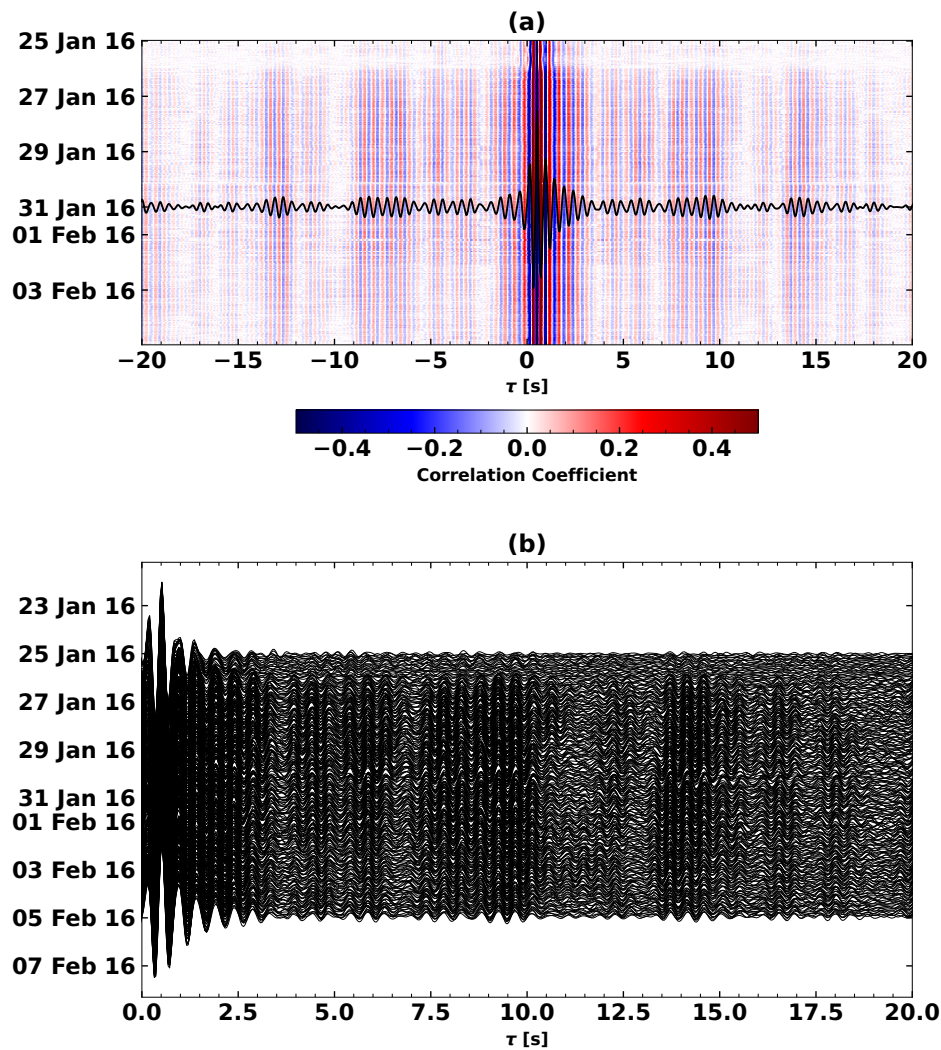


Figure 5 Hourly autocorrelations of ambient noise at X9.IR1. This plot showcases two styles to plot correlations in SeisMIC. **(a)** Autocorrelations plotted as a colour image. The colours scale with the amplitude of the correlation. We superimpose the average of all shown autocorrelations on top of the heatmap. **(b)** Autocorrelations plotted as a section plot. In this plot, each hourly CF corresponds to one curve. Here, we only show the causal side of the CF.

284 2023b). Therefore, we henceforth focus on the analysis of dv/v between 2 and 4 Hz.

285 3.4 Computing Velocity Changes Using the Stretching Method

286 Using the procedure theoretically outlined in section 2.2, we can estimate the evolution of the seismic velocity in
 287 the study period. Like previously, the parametrisation is handled over the *YAML* file (see supplementary material).
 288 Before computing dv/v , we smooth the one-hour CFs with a 4-hour long Hanning window. As reference CF, we use
 289 the mean of all CFs. Then, we compute dv/v for lag times between 3.5 s and 12 s simultaneously from the causal and
 290 acausal parts of the coda. We plot the resulting velocity change time series using one of SeisMIC's standard plotting
 291 templates in Figure 7.

292 Even though we do not focus on data interpretation in this article, we should take a brief look at the presented
 293 results. Most notably, we identify a clear velocity drop coinciding with the regional M7.2 Zhupanov earthquake.
 294 Interestingly, the resolution of the dv/v time series is high enough to identify a diurnal cycle that could be caused
 295 by air temperature and pressure variations, for example, observed by Wang et al. (2020), or be due to lunar and
 296 solar tides as reported by Yamamura et al. (2003) and Sens-Schönfelder and Eulenfeld (2019). Lastly, we note that the

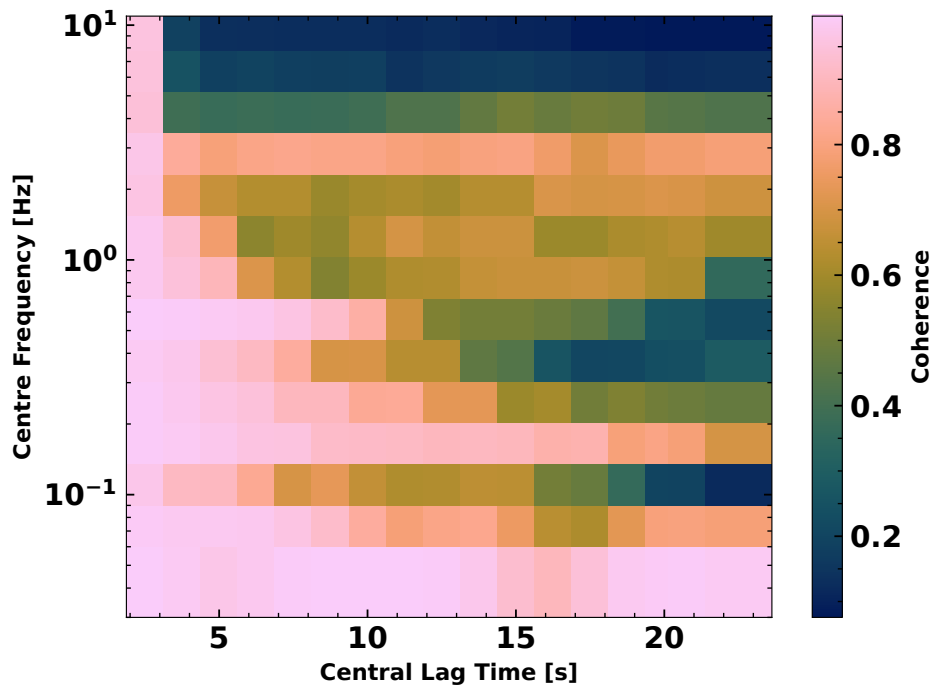


Figure 6 The waveform coherence as a function of lag time and frequency for the dataset from station X9.IR1 and channel HHE. For details, consult the text body.

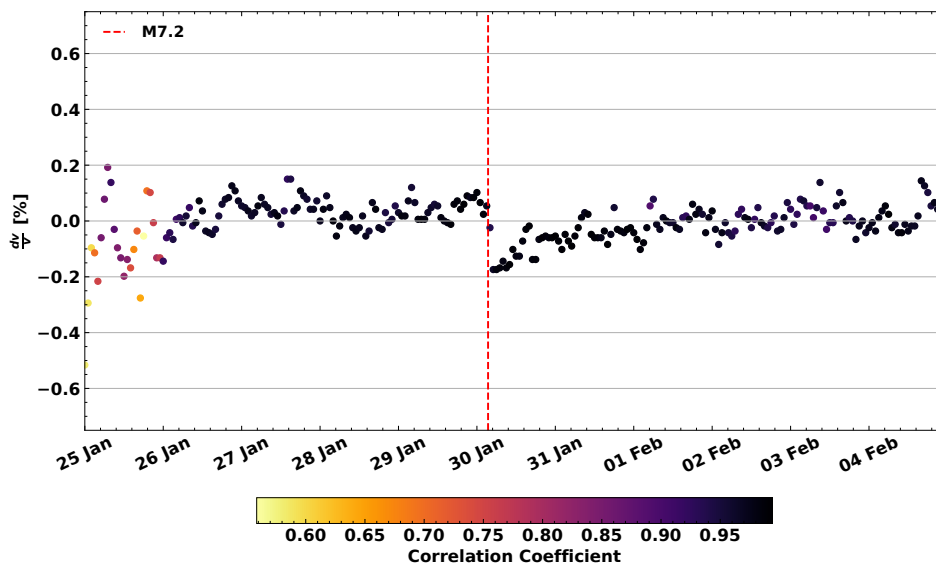


Figure 7 Velocity change time series estimated from the CFs shown in Figure 5. The increment between each data point is one hour and the shown dv/v is derived from CFs that are smoothed over 4 hours. The points' colour scales with the correlation coefficient (coherence) between the stretched CF and the reference CF. We plotted the origin time of the M7.2 Zhupanov earthquake as a vertical red line. An obvious velocity drop coinciding with the event can be identified. A subsequent recovery and more subtle differences in seismic velocity between day- and nighttime are visible.

297 correlation coefficient is significantly lower before 26 January 2016. We link this observation to a transient change in
 298 the wavefield as described by Makus et al. (2023b) and Steinmann et al. (2023).

299 3.5 Spatial Imaging of Velocity Changes

300 Velocity change estimates like the one presented in Figure 7 show dv/v as a function of time but do not directly
 301 yield insight into the spatial distribution of these velocity changes. The spatially extended sampling of coda waves
 302 increases the sensitivity to distributed weak velocity changes and the detectability of localised changes but prevents

303 a simple inference of the affected location along a ray path or Fresnel volume. The affected location can, however,
304 be estimated using sensitivity kernels that describe the time-dependent energy distribution of the wavefield for a
305 statistically uniform medium. For a theoretical derivation of the sensitivity kernels based on the Radiative Transfer
306 Theory, refer to [Mayor et al. \(2014\)](#), [Margerin et al. \(2016\)](#), and [Zhang et al. \(2022\)](#).

307 In SeisMIC, we implemented a simplified approach relying on sensitivity kernels derived from an approximate
308 solution of the Boltzmann equation for a homogeneous medium ([Paasschens, 1997](#)) describing isotropic scattering
309 of acoustic waves. Using these sensitivity kernels and a linearised inversion scheme proposed by [Obermann et al.](#)
310 ([2013b](#)), we can map a 2-dimensional distribution of dv/v at a fixed time t_i resulting in $dv/v(t_i, x, y)$.

311 In SeisMIC, the module `seismic.monitor.spatial` contains the necessary functions for the outlined approach.
312 To illustrate the procedure and make our example easily adaptable and reproducible, we create a synthetic velocity-
313 change model, which we then forward model onto a random station configuration. After adding noise to the synthetic
314 data, we try to recover the initial model using the inverse algorithm. In detail, we proceed as follows: First, we create
315 a synthetic velocity change model with an extent of $40 \text{ km} \times 40 \text{ km}$ and a spatial resolution of 1 km (Figures 8 (b) and
316 (d)). The background medium has a homogeneous velocity of $3 \frac{\text{km}}{\text{s}}$ and a transport mean free path l_0 of 30 km. Then,
317 we place an arbitrary number of stations on random positions along the grid. Using sensitivity kernels of cross-
318 and autocorrelations, we solve the forward problem to compute dv/v , as it would be obtained from the CFs in the
319 presence of the spatial velocity variations. The sensitivity kernels are computed for lapse time windows between 14
320 and 34 s. To the dv/v values, we add random noise. This noise follows a Gaussian distribution around 0% velocity
321 change with a standard deviation of 0.1%. Finally, we invert for the synthetic model employing the damped linearised
322 inversion ([Obermann et al., 2013b](#)). We show the results of this inversion in Figures 8 (a) and (c) for 4 and 32 stations,
323 respectively. There, we also indicate the used damping parameters. The optimal damping parameters minimise both
324 the misfit between the initial and the retrieved model and the model complexity and can be found using the L-curve
325 criterion, as discussed by [Obermann et al. \(2013b\)](#).

326 The results demonstrate that increasing the number of stations is the most powerful tool to decrease the misfit
327 between the inversion result and the input model. While the geometry of the synthetic model is poorly retrieved for
328 a configuration using only four stations, we can reproduce the model quite accurately with 32 stations.

329 The supplementary material contains a Jupyter notebook to reproduce or modify these results with an arbitrary
330 number of stations, velocity change model, and damping parameters. We also include options to invert for dv/v
331 only utilising data from auto- or cross-correlations and using sensitivity kernels from split coda windows (i.e., with
332 lapse time windows sliced into narrow sub-windows). In the supplement, we show results that exploit these options.
333 Based on these, we argue that adding dv/v information from auto- and cross-correlations, improves the accuracy of
334 the result notably, whereas splitting the coda yields only minor improvements.

335 4 Conclusion and Outlook

336 We presented SeisMIC, a software to estimate changes in the seismic propagation velocity from continuous records
337 of seismic ambient noise. SeisMIC contains functionalities for the end-to-end processing of velocity-change time
338 series, including data retrieval, the computation of correlation functions, calculating velocity change time series

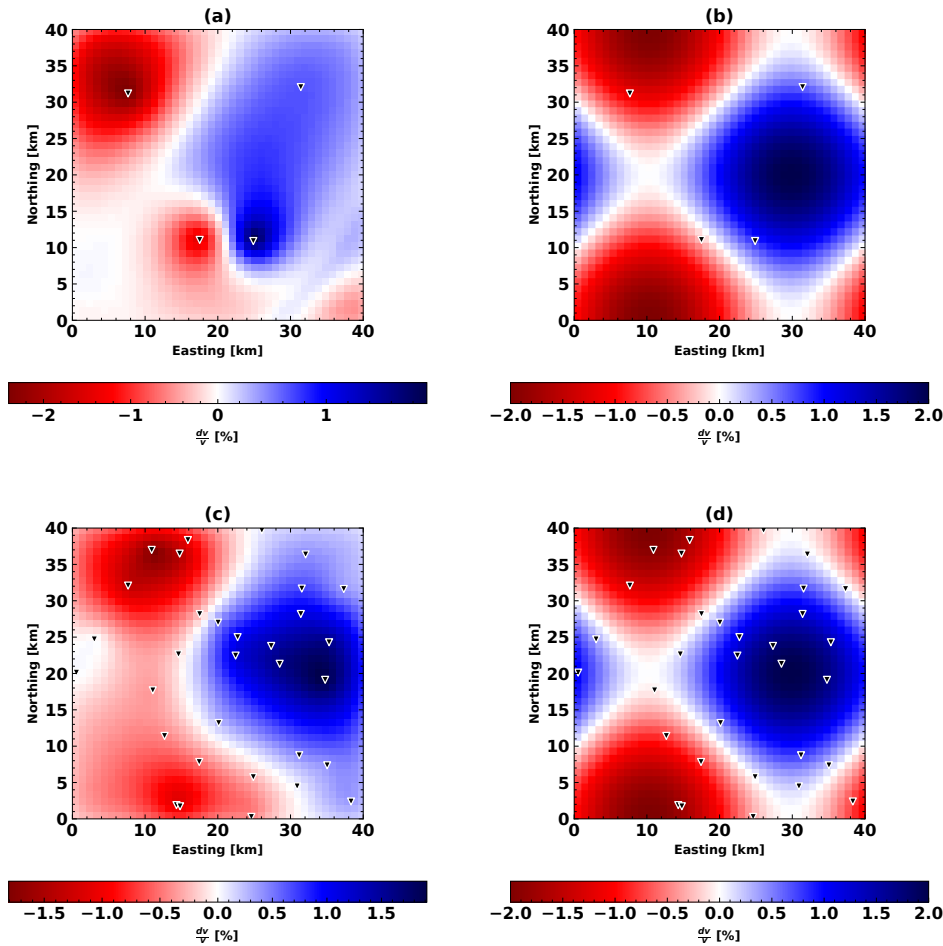


Figure 8 Two examples of the spatial inversion using different parametrisations and station configurations. **(a)** Result of the spatial inversion algorithm using four stations, a model variance $\sigma_m = 0.1 \frac{\text{km}}{\text{km}^2}$, and a correlation length $\lambda = 2$ km. **(b)** The synthetic velocity model and station configuration used to obtain (a). **(c)** Result of the spatial inversion algorithm using 32 stations, $\sigma_m = 0.01 \frac{\text{km}}{\text{km}^2}$, and $\lambda = 2$ km. **(d)** The synthetic velocity model and station configuration used to obtain (c). For an exhaustive description of the parametrisation and the inversion steps, consult the text body.

339 using the stretching method, and postprocessing as well as inverting dv/v time series onto a spatial grid. While these
 340 functions can be part of a workflow, they are also intended to be used separately and can easily be altered and adapted
 341 to individual processes.

342 In the near future, we will release versions capable of estimating dv/v employing algorithms other than the
 343 stretching method, like the wavelet-cross-spectrum analysis (Mao et al., 2020). Other future milestones include ex-
 344 ploiting the computational power of GPUs to decrease the compute time of noise correlations even further and adding
 345 solutions that automatically update correlation function databases.

346 SeisMIC complements existing software to process ambient noise. Highlights are its broad functionality, high ef-
 347 ficiency, and versatility applicable to local small-scale studies on a laptop computer as well as surveys using large-N
 348 arrays processed on computer clusters. SeisMIC is available on GitHub as a well-documented and regularly main-
 349 tained open-source software.

350 Acknowledgements

351 We thank Luc Illien, Ugo Nanni, Jannes Münchmeyer, Marine Denolle, Charlotte Bruland, Tuo Zhang, and Raphael
 352 De Plaen for discussions that helped improving this software. This work was supported by the DFG grant SE1844/12-1.

Data and code availability

This manuscript is distributed with a supporting information in PDF format. Aside from the supporting document, we provide Jupyter notebooks, computing scripts, and the main program "SeisMIC" as a digital supplement. For SeisMIC, however, we strongly encourage the reader to obtain the code's latest version, for example, from GitHub. The digital supplement includes SeisMIC 0.5.3 and is available at <https://doi.org/10.5281/zenodo.8283683>.

The SeisMIC data from the KISS experiment (Shapiro et al., 2017) used in section 3 can be obtained from the GE-OFON webservice (Quinteros et al., 2021). For the benchmarks in section 2.3, we used data from the Saxony Network (University of Leipzig, 2001) available from the EIDA FDSN service (Strollo et al., 2021).

Competing interests

The authors do not declare any competing interests.

References

- Arrowsmith, S. J., Trugman, D. T., MacCarthy, J., Bergen, K. J., Lumley, D., and Magnani, M. B. Big Data Seismology. *Reviews of Geophysics*, 60(2):e2021RG000769, 2022. doi: 10.1029/2021RG000769.
- Asnar, M., Sens-Schönfelder, C., Bonnelye, A., and Dresen, G. Non-Classical, Non-Linear Elasticity in Rocks: Experiments in a Triaxial Cell with Pore Pressure Control. Technical Report EGU23-8050, Copernicus Meetings, Feb. 2023.
- Barbe, K., Pintelon, R., and Schoukens, J. Welch Method Revisited: Nonparametric Power Spectrum Estimation Via Circular Overlap. *IEEE Transactions on Signal Processing*, 58(2):553–565, Feb. 2010. doi: 10.1109/TSP.2009.2031724.
- Bensen, G. D., Ritzwoller, M. H., Barmin, M. P., Levshin, A. L., Lin, F., Moschetti, M. P., Shapiro, N. M., and Yang, Y. Processing Seismic Ambient Noise Data to Obtain Reliable Broad-Band Surface Wave Dispersion Measurements. *Geophysical Journal International*, 169(3):1239–1260, 2007. doi: 10.1111/j.1365-246X.2007.03374.x.
- Beyreuther, M., Barsch, R., Krischer, L., Megies, T., Behr, Y., and Wassermann, J. ObsPy: A Python Toolbox for Seismology. *Seismological Research Letters*, 81(3):530–533, May 2010. doi: 10.1785/gssrl.81.3.530.
- Bièvre, G., Franz, M., Larose, E., Carrière, S., Jongmans, D., and Jaboyedoff, M. Influence of Environmental Parameters on the Seismic Velocity Changes in a Clayey Mudflow (Pont-Bourquin Landslide, Switzerland). *Engineering Geology*, 245:248–257, Nov. 2018. doi: 10.1016/j.enggeo.2018.08.013.
- Brenguier, F., Campillo, M., Hadziioannou, C., Shapiro, N. M., Nadeau, R. M., and Larose, E. Postseismic Relaxation Along the San Andreas Fault at Parkfield from Continuous Seismological Observations. *Science*, 321(5895):1478–1481, Sept. 2008. doi: 10.1126/science.1160943.
- Clements, T. and Denolle, M. A. Tracking Groundwater Levels Using the Ambient Seismic Field. *Geophysical Research Letters*, 45(13):6459–6465, 2018. doi: 10.1029/2018GL077706.
- Clements, T. and Denolle, M. A. SeisNoise.Jl: Ambient Seismic Noise Cross Correlation on the CPU and GPU in Julia. *Seismological Research Letters*, 92(1):517–527, 2021. doi: 10.1785/0220200192.
- Clymer, R. W. and McEvelly, T. V. Travel-Time Monitoring with Vibroseis*. *Bulletin of the Seismological Society of America*, 71(6):1903–1927, Dec. 1981. doi: 10.1785/BSSA0710061903.
- Collette, A., Kluyver, T., Caswell, T. A., Tocknell, J., Kieffer, J., Scopatz, A., Dale, D., Chen, Jelenak, A., payno, juliagarriga, VINCENT, T., Sciarelli,

- 388 P., Valls, V., Kofoed Pedersen, U., jakirkham, Raspaud, M., Parsons, A., Abbasi, H., Readey, J., Paramonov, A., Chan, L., jialin, Danilevski, C.,
389 Feng, Y., Vaillant, G. A., Teichmann, M., Brucher, M., Johnson, S. R., and Hole, L. H5py/H5py: 3.1.0. *Zenodo*, Nov. 2020. doi: 10.5281/zen-
390 odo.4250762.
- 391 Dalcin, L. and Fang, Y.-L. L. Mpi4py: Status Update After 12 Years of Development. *Computing in Science & Engineering*, 23(4):47–54, July
392 2021. doi: 10.1109/MCSE.2021.3083216.
- 393 Donaldson, C., Winder, T., Caudron, C., and White, R. S. Crustal Seismic Velocity Responds to a Magmatic Intrusion and Seasonal Loading
394 in Iceland’s Northern Volcanic Zone. *Science Advances*, 5(11):eaax6642, Nov. 2019. doi: 10.1126/sciadv.aax6642.
- 395 Harris, C. R., Millman, K. J., van der Walt, S. J., Gommers, R., Virtanen, P., Cournapeau, D., Wieser, E., Taylor, J., Berg, S., Smith, N. J., Kern,
396 R., Picus, M., Hoyer, S., van Kerkwijk, M. H., Brett, M., Haldane, A., del Río, J. F., Wiebe, M., Peterson, P., Gérard-Marchant, P., Sheppard, K.,
397 Reddy, T., Weckesser, W., Abbasi, H., Gohlke, C., and Oliphant, T. E. Array Programming with NumPy. *Nature*, 585(7825):357–362, Sept.
398 2020. doi: 10.1038/s41586-020-2649-2.
- 399 Hirose, T., Nakahara, H., and Nishimura, T. Combined Use of Repeated Active Shots and Ambient Noise to Detect Temporal Changes in
400 Seismic Velocity: Application to Sakurajima Volcano, Japan 4. *Seismology. Earth, Planets and Space*, 69(1), 2017. doi: 10.1186/s40623-
401 017-0613-7.
- 402 Hong, N. P. C., Katz, D. S., Barker, M., Lamprecht, A.-L., Martinez, C., Psomopoulos, F. E., Harrow, J., Castro, L. J., Gruenpeter, M., Mar-
403 tinez, P. A., Honeyman, T., Struck, A., Lee, A., Loewe, A., van Werkhoven, B., Garijo, D., Plomp, E., Genova, F., Shanahan, H., Hellström,
404 M., Sandström, M., Sinha, M., Kuzak, M., Herterich, P., Islam, S., Sansone, S.-A., Pollard, T., Atmojo, U. D., Williams, A., Czerniak, A.,
405 Niehues, A., Fouilloux, A. C., Desinghu, B., Goble, C., Richard, C., Gray, C., Erdmann, C., Nüst, D., Tartarini, D., Ranguelova, E., Anzt, H.,
406 Todorov, I., McNally, J., Burnett, J., Garrido-Sánchez, J., Belhajjame, K., Sesink, L., Hwang, L., Tovani-Palone, M. R., Wilkinson, M. D.,
407 Servillat, M., Liffers, M., Fox, M., Miljković, N., Lynch, N., Lavanchy, P. M., Gesing, S., Stevens, S., Cuesta, S. M., Peroni, S., Soiland-Reyes,
408 S., Bakker, T., Rabemanantsoa, T., Sochat, V., Yehudi, Y., and Wg, F. FAIR Principles for Research Software (FAIR4RS Principles). Mar. 2022.
409 doi: 10.15497/RDA00065.
- 410 Hunter, J. D. Matplotlib: A 2D Graphics Environment. *Computing in Science & Engineering*, 9(03):90–95, May 2007. doi: 10.1109/M-
411 CSE.2007.55.
- 412 Ikuta, R., Yamaoka, K., Miyakawa, K., Kunitomo, T., and Kumazawa, M. Continuous Monitoring of Propagation Velocity of Seismic Wave
413 Using ACROSS. *Geophysical Research Letters*, 29(13):5–1–5–5, 2002. doi: 10.1029/2001GL013974.
- 414 Illien, L., Andermann, C., Sens-Schönfelder, C., Cook, K. L., Baidya, K. P., Adhikari, L. B., and Hovius, N. Subsurface Moisture Regulates
415 Himalayan Groundwater Storage and Discharge. *AGU Advances*, 2(2), 2021. doi: 10.1029/2021av000398.
- 416 Jiang, C. and Denolle, M. A. Noisepy: A New High-Performance Python Tool for Ambient-Noise Seismology. *Seismological Research Letters*,
417 91(3):1853–1866, 2020. doi: 10.1785/0220190364.
- 418 Koranne, S. Hierarchical Data Format 5 : HDF5. In Koranne, S., editor, *Handbook of Open Source Tools*, pages 191–200. Springer US, Boston,
419 MA, 2011.
- 420 Lecocq, T., Caudron, C., and Brenguier, F. MSNoise, a Python Package for Monitoring Seismic Velocity Changes Using Ambient Seismic
421 Noise. *Seismological Research Letters*, 85(3):715–726, May 2014. doi: 10.1785/0220130073.
- 422 Lindner, F., Wassermann, J., and Igel, H. Seasonal Freeze-Thaw Cycles and Permafrost Degradation on Mt. Zugspitze (German/Austrian Alps)
423 Revealed by Single-Station Seismic Monitoring. *Geophysical Research Letters*, 48(18):e2021GL094659, 2021. doi: 10.1029/2021GL094659.
- 424 Makus, P. and Sens-Schönfelder, C. Seismological Monitoring Using Interferometric Concepts (SeisMIC). GFZ Data Services, 2022.
- 425 Makus, P., Denolle, M., Sens-Schönfelder, C., Köpfli, M., and Tilmann, F. The Complex Relationship between Seismic Velocity and Volcanic,

- 426 Tectonic, and Environmental Forcings Illustrated by 23 Years of Data at Mt. St. Helens. In *EGU23*. Copernicus Meetings, Feb. 2023a.
427 doi: 10.5194/egusphere-egu23-6757.
- 428 Makus, P., Sens-Schönfelder, C., Illien, L., Walter, T. R., Yates, A., and Tilmann, F. Deciphering the Whisper of Volcanoes: Monitoring Ve-
429 locity Changes at Kamchatka's Klyuchevskoy Group With Fluctuating Noise Fields. *Journal of Geophysical Research: Solid Earth*, 128(4):
430 e2022JB025738, 2023b. doi: 10.1029/2022JB025738.
- 431 Mao, S., Mordret, A., Campillo, M., Fang, H., and van der Hilst, R. D. On the Measurement of Seismic Traveltime Changes in the
432 Time-Frequency Domain with Wavelet Cross-Spectrum Analysis. *Geophysical Journal International*, 221(1):550–568, Apr. 2020.
433 doi: 10.1093/gji/ggz495.
- 434 Mao, S., Lecointre, A., van der Hilst, R. D., and Campillo, M. Space-Time Monitoring of Groundwater Fluctuations with Passive Seismic
435 Interferometry. *Nature Communications*, 13(1):4643, Aug. 2022. doi: 10.1038/s41467-022-32194-3.
- 436 Margerin, L., Planès, T., Mayor, J., and Calvet, M. Sensitivity Kernels for Coda-Wave Interferometry and Scattering Tomography: Theory and
437 Numerical Evaluation in Two-Dimensional Anisotropically Scattering Media. *Geophysical Journal International*, 204(1):650–666, Jan.
438 2016. doi: 10.1093/gji/ggv470.
- 439 Mayor, J., Margerin, L., and Calvet, M. Sensitivity of Coda Waves to Spatial Variations of Absorption and Scattering: Radiative Transfer
440 Theory and 2-D Examples. *Geophysical Journal International*, 197(2):1117–1137, May 2014. doi: 10.1093/gji/ggu046.
- 441 Minato, S., Tsuji, T., Ohmi, S., and Matsuoka, T. Monitoring Seismic Velocity Change Caused by the 2011 Tohoku-oki Earthquake Using
442 Ambient Noise Records. *Geophysical Research Letters*, 39(9), 2012. doi: 10.1029/2012GL051405.
- 443 Mordret, A., Mikesell, T. D., Harig, C., Lipovsky, B. P., and Prieto, G. A. Monitoring Southwest Greenland's Ice Sheet Melt with Ambient Seismic
444 Noise. *Science Advances*, 2(5):e1501538, May 2016. doi: 10.1126/sciadv.1501538.
- 445 Nanni, U., Pauze, T., Goulet, L., Köhler, A., Bouchayer, C., and Schuler, T. Study of the Structural and Dynamic Changes of a Surging Glacier
446 Using Seismic Observations. In *IUGG*, Berlin, July 2023.
- 447 Nishimura, T., Uchida, N., Sato, H., Ohtake, M., Tanaka, S., and Hamaguchi, H. Temporal Changes of the Crustal Structure Associated with
448 the M6.1 Earthquake on September 3, 1998, and the Volcanic Activity of Mount Iwate, Japan. *Geophysical Research Letters*, 27(2):269–272,
449 2000. doi: 10.1029/1999GL005439.
- 450 Obermann, A., Planès, T., Larose, E., and Campillo, M. Imaging Preeruptive and Coeruptive Structural and Mechanical Changes of a Volcano
451 with Ambient Seismic Noise. *Journal of Geophysical Research: Solid Earth*, 118(12):6285–6294, 2013a. doi: 10.1002/2013JB010399.
- 452 Obermann, A., Planès, T., Larose, E., and Campillo, M. Imaging Preeruptive and Coeruptive Structural and Mechanical Changes of a Volcano
453 with Ambient Seismic Noise. *Journal of Geophysical Research: Solid Earth*, 118(12):6285–6294, 2013b. doi: 10.1002/2013JB010399.
- 454 Paasschens, J. C. J. Solution of the Time-Dependent Boltzmann Equation. *Physical Review E*, 56(1):1135–1141, July 1997. doi: 10.1103/Phys-
455 RevE.56.1135.
- 456 Poupinet, G., Ellsworth, W. L., and Frechet, J. Monitoring Velocity Variations in the Crust Using Earthquake Doublets: An Application to the
457 Calaveras Fault, California. *Journal of Geophysical Research: Solid Earth*, 89(B7):5719–5731, July 1984. doi: 10.1029/JB089iB07p05719.
- 458 Quinteros, J., Strollo, A., Evans, P. L., Hanka, W., Heinloo, A., Hemmleb, S., Hillmann, L., Jaeckel, K.-H., Kind, R., Saul, J., Zieke, T., and
459 Tilmann, F. The GEOFON Program in 2020. *Seismological Research Letters*, 92(3):1610–1622, Feb. 2021. doi: 10.1785/0220200415.
- 460 Sawazaki, K., Kimura, H., Shiomi, K., Uchida, N., Takagi, R., and Snieder, R. Depth-Dependence of Seismic Velocity Change Associated with
461 the 2011 Tohoku Earthquake, Japan, Revealed from Repeating Earthquake Analysis and Finite-Difference Wave Propagation Simulation.
462 *Geophysical Journal International*, 201(2):741–763, May 2015. doi: 10.1093/gji/ggv014.
- 463 Sens-Schönfelder, C. and Eulenfeld, T. Probing the in Situ Elastic Nonlinearity of Rocks with Earth Tides and Seismic Noise. *Physical Review*

- 464 *Letters*, 122(13):138501, Apr. 2019. doi: 10.1103/PhysRevLett.122.138501.
- 465 Sens-Schönfelder, C. and Wegler, U. Passive Image Interferometry and Seasonal Variations of Seismic Velocities at Merapi Volcano, Indone-
466 sia. *Geophysical Research Letters*, 33(21):1–5, 2006. doi: 10.1029/2006GL027797.
- 467 Sens-Schönfelder, C. and Wegler, U. Passive Image Interferometry for Monitoring Crustal Changes with Ambient Seismic Noise. *Comptes*
468 *Rendus Geoscience*, 343(8):639–651, Sept. 2011. doi: 10.1016/j.crte.2011.02.005.
- 469 Sens-Schönfelder, C., Flores-Estrella, H., Gassenmeier, M., Korn, M., Köllner, F., Milkereit, C., Niederleithinger, E., Parolai, S., Pilz, M., Pom-
470 poni, E., Schuck, A., Thiemann, K., and Völkel, J. MIIC: Monitoring and Imaging Based on Interferometric Concepts. In Weber, M. and
471 Münch, U., editors, *Tomography of the Earth's Crust: From Geophysical Sounding to Real-Time Monitoring: GEOTECHNOLOGIEN Science*
472 *Report No. 21*, Advanced Technologies in Earth Sciences, pages 43–61. Springer International Publishing, Cham, 2014a.
- 473 Sens-Schönfelder, C., Pomponi, E., and Peltier, A. Dynamics of Piton de La Fournaise Volcano Observed by Passive Image Interferometry
474 with Multiple References. *Journal of Volcanology and Geothermal Research*, 276:32–45, 2014b. doi: 10.1016/j.jvolgeores.2014.02.012.
- 475 Shapiro, N., Sens-Schönfelder, C., Lühr, B., Weber, M., Abkadyrov, I., Gordeev, E., Koulakov, I., Jakovlev, A., Kugaenko, Y., and Saltykov, V.
476 Understanding Kamchatka's Extraordinary Volcano Cluster. *Eos*, May 2017. doi: 10.1029/2017EO071351.
- 477 Snieder, R., Grêt, A., Douma, H., and Scales, J. Coda Wave Interferometry for Estimating Nonlinear Behavior in Seismic Velocity. *Science*,
478 295(5563):2253–2255, 2002. doi: 10.1126/science.1070015.
- 479 Steinmann, R., Hadziioannou, C., and Larose, E. Effect of Centimetric Freezing of the near Subsurface on Rayleigh and Love Wave Velocity
480 in Ambient Seismic Noise Correlations. *Geophysical Journal International*, 224(1):626–636, 2021. doi: 10.1093/gji/ggaa406.
- 481 Steinmann, R., Seydoux, L., Journeau, C., Shapiro, N. M., and Campillo, M. Machine Learning Analysis of Seismograms Reveals a Continuous
482 Plumbing System Evolution beneath the Klyuchevskoy Volcano in Kamchatka, Russia, June 2023.
- 483 Strollo, A., Cambaz, D., Clinton, J., Danecek, P., Evangelidis, C. P., Marmureanu, A., Ottemöller, L., Pedersen, H., Sleeman, R., Stammer,
484 K., Armbruster, D., Bienkowski, J., Boukouras, K., Evans, P. L., Fares, M., Neagoe, C., Heimers, S., Heinloo, A., Hoffmann, M., Kaestli, P.,
485 Lauciani, V., Michalek, J., Odon Muhire, E., Ozer, M., Palangeanu, L., Pardo, C., Quinteros, J., Quintiliani, M., Antonio Jara-Salvador, J.,
486 Schaeffer, J., Schloemer, A., and Triantafyllis, N. EIDA: The European Integrated Data Archive and Service Infrastructure within ORFEUS.
487 *Seismological Research Letters*, 92(3):1788–1795, Mar. 2021. doi: 10.1785/0220200413.
- 488 University of Leipzig. SXNET Saxon Seismic Network, 2001.
- 489 Virtanen, P., Gommers, R., Oliphant, T. E., Haberland, M., Reddy, T., Cournapeau, D., Burovski, E., Peterson, P., Weckesser, W., Bright, J., van
490 der Walt, S. J., Brett, M., Wilson, J., Millman, K. J., Mayorov, N., Nelson, A. R. J., Jones, E., Kern, R., Larson, E., Carey, C. J., Polat, İ., Feng,
491 Y., Moore, E. W., VanderPlas, J., Laxalde, D., Perktold, J., Cimrman, R., Henriksen, I., Quintero, E. A., Harris, C. R., Archibald, A. M., Ribeiro,
492 A. H., Pedregosa, F., and van Mulbregt, P. SciPy 1.0: Fundamental Algorithms for Scientific Computing in Python. *Nature Methods*, 17(3):
493 261–272, Mar. 2020. doi: 10.1038/s41592-019-0686-2.
- 494 Wang, B., Yang, W., Wang, W., Yang, J., Li, X., and Ye, B. Diurnal and Semidiurnal P- and S-Wave Velocity Changes Measured Using an Airgun
495 Source. *Journal of Geophysical Research: Solid Earth*, 125(1):e2019JB018218, 2020. doi: 10.1029/2019JB018218.
- 496 Wang, Q. Y., Brenguier, F., Campillo, M., Lecointre, A., Takeda, T., and Aoki, Y. Seasonal Crustal Seismic Velocity Changes Throughout Japan.
497 *Journal of Geophysical Research: Solid Earth*, 122(10):7987–8002, 2017. doi: 10.1002/2017JB014307.
- 498 Wegler, U., Lühr, B. G., Snieder, R., and Ratdomopurbo, A. Increase of Shear Wave Velocity before the 1998 Eruption of Merapi Volcano
499 (Indonesia). *Geophysical Research Letters*, 33(9):4–7, 2006. doi: 10.1029/2006GL025928.
- 500 Wu, C., Tan, X., Li, H., and Sun, G. An Efficient Ambient Noise Cross-Correlation Algorithm on Heterogeneous CPU-GPU Cluster.
501 In *2022 IEEE 13th International Symposium on Parallel Architectures, Algorithms and Programming (PAAP)*, pages 1–5, Nov. 2022.

502 doi: 10.1109/PAAP56126.2022.10010612.

503 Yamamura, K., Sano, O., Utada, H., Takei, Y., Nakao, S., and Fukao, Y. Long-Term Observation of in Situ Seismic Velocity and Attenuation.

504 *Journal of Geophysical Research: Solid Earth*, 108(B6), 2003. doi: 10.1029/2002JB002005.

505 Yang, W., Wang, B., Yuan, S., and Ge, H. Temporal Variation of Seismic-Wave Velocity Associated with Groundwater Level Observed by a

506 Downhole Airgun near the Xiaojiang Fault Zone. *Seismological Research Letters*, 89(3):1014–1022, Apr. 2018. doi: 10.1785/0220170282.

507 Zhang, H., Glasgow, M., Schmandt, B., Thelen, W. A., Moran, S. C., and Thomas, A. M. Revisiting the Depth Distribution of Seismicity be-

508 fore and after the 2004–2008 Eruption of Mount St. Helens. *Journal of Volcanology and Geothermal Research*, 430:107629, Oct. 2022.

509 doi: 10.1016/j.jvolgeores.2022.107629.

Supporting Information for "SeisMIC - an Open Source Python Toolset to Compute Velocity Changes from Ambient Seismic Noise"

Peter Makus *,^{1,2}, Christoph Sens-Schönfelder ¹

¹Helmholtz Center, German Research Center for Geosciences GFZ, Potsdam, Germany, ²Institute for Geological Sciences, Freie Universität Berlin, Berlin, Germany

1 Introduction

In this supporting information, we elaborate on the approximation of the stretching factor implemented in SeisMIC. We show a short derivation in section 2.

In section 3, we present selected results of the spatial inversion procedure to illustrate the effect of (1) subdividing the coda to obtain several independent velocity change estimates (hereafter referred to as coda splitting) and (2) adding information from autocorrelations and cross-station correlations to the analysis. To this end, we provide several examples using different station configurations and damping parameters. For a thorough discussion of the algorithm, please refer to the main manuscript. The reader can reproduce and extend the shown results using the `spatial.ipynb` Jupyter notebook provided in the digital supplement.

For the coda splitting, we split the total of the used coda window into three equally long subwindows and obtain one sensitivity kernel for each subwindow. That is when exploiting the coda splitting, we compute separate sensitivity kernels for lapse times from 14 to 20.66 s, from 20.66 s to 27.33 s, and from 27.33 s to 34 s, whereas without coda splitting, we only obtain one sensitivity kernel representing lag times from 14 s to 34 s. To all forward-modelled dv/v results, we add random noise from a Gaussian distribution with a standard deviation of only 0.05% dv/v to the predicted velocity changes to render the comparison less dependent on the noise level. Otherwise, the procedure for the spatial inversion remains identical to the one described in the main manuscript section 3.5.

Apart from this supporting document, we provide Jupyter notebooks, computing scripts, and the main program, SeisMIC 0.5.3, as a digital supplement. For SeisMIC, however, we strongly encourage the reader to obtain the code's latest version, for example, from GitHub. For details about where to retrieve these additional supplements, please refer to the *data and code availability* section in the main manuscript.

2 Derivation of the Stretching

A problem with the commonly used definition of a velocity change dv/v is that it is neither additive nor reversible, i.e. $dv/v_{A \rightarrow B} \neq -dv/v_{B \rightarrow A}$ because the reference velocity of the two measurements may be different and the com-

*Corresponding author: makus@gfz-potsdam.de

32 monly used equation $dv/v = -dt/t$ is an approximation for small dv/v . Even though the error is small, we can reduce
 33 it further with a different definition of the velocity change. This is especially useful for smoothing, averaging, or
 34 otherwise manipulating velocity change time series.

35 Assuming infinite frequency (i.e., ray theory), the travel time $t(\mathbf{x})$ of a wave travelling from point \mathbf{x}_1 to \mathbf{x}_2 through
 36 any medium is given by:

$$37 \quad t(\mathbf{x}) = \int_{\mathbf{x}_1}^{\mathbf{x}_2} \frac{1}{v(\mathbf{x})} d\mathbf{x} \quad (1)$$

38 where $v(\mathbf{x})$ is the velocity at point \mathbf{x} . If we assume a medium with a homogeneous velocity, i.e., $v(\mathbf{x}) = v$, equation 1
 39 simplifies to:

$$40 \quad t = \frac{\Delta x}{v} \quad (2)$$

41 where $\Delta x = \|\mathbf{x}_1 - \mathbf{x}_2\|$ is the Euclidean distance which remains constant throughout. In interferometry, we examine
 42 the case where the velocity $v(t)$ is variable with time. To quantify the change in velocity, we compare the velocity of
 43 a reference state $\tilde{v} = \Delta x/\tilde{t}$ with the velocity $v' = \Delta x/t'$ in a perturbed state. Due to the constant Δx , we obtain from
 44 equation 2:

$$45 \quad \frac{\tilde{t}}{t'} = \frac{v'}{\tilde{v}} = \xi \quad (3)$$

46 defining the stretching factor ξ .

We seek a transformation

$$\mathcal{S}(\kappa) : \tilde{t} \mapsto t' = \frac{1}{\xi} \tilde{t}$$

that maps the original travel times \tilde{t} of the seismic waves through the unperturbed medium to the travel times t'
 through the perturbed medium. This transformation shall have the following property:

$$\mathcal{S}(\kappa_1)\mathcal{S}(\kappa_2) = \mathcal{S}(\kappa_1 + \kappa_2)$$

to ensure that stretching is additive and reversible. We choose

$$\xi = e^\kappa$$

to calculate the stretching factor. We satisfy the above requirement for any combination of reference and perturbed
 states since $e^{\kappa_1} * e^{\kappa_2} = e^{\kappa_1 + \kappa_2}$. In SeisMIC, we implement $\xi = e^\kappa$ to guarantee the linearity in the processing. To
 interpret measurements in the usual way as fractional velocity change, we use the approximation

$$\frac{dv}{v} = \frac{v' - \tilde{v}}{\tilde{v}} = \xi - 1 \approx \kappa$$

47 .

48 Utilising $\xi = 1 + \frac{dv}{v}$ for processing introduces nonlinearities and a dependency on the reference state. We note
 49 that this effect is not limited to measurements of the velocity change with the stretching method. Any manipulation
 50 of $\frac{dv}{v}$ is affected and can be improved by working with $\kappa = \log(v'/\tilde{v})$.

51 **3 Additional Results of the Synthetic Spatial Imaging**

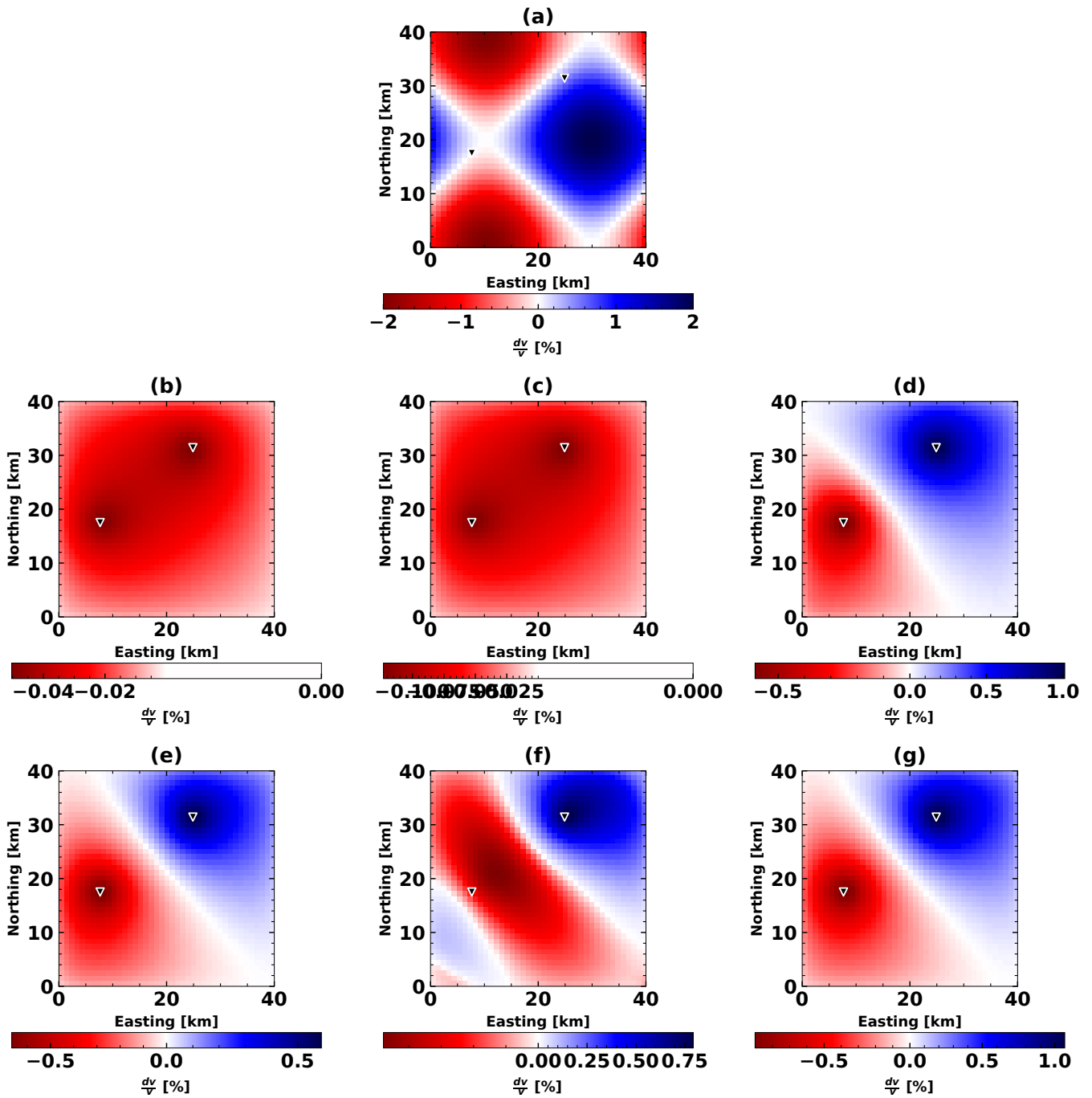


Figure 1 Examples of the spatial inversion using data from two stations, a model variance $\sigma_m = 0.5 \frac{\text{km}}{\text{km}^2}$, and a correlation length $\lambda = 2 \text{ km}$. **(a)** The synthetic velocity model and station configuration used. **(b)** Result of the spatial inversion using only cross-correlations and a single lapse time window. **(c)** Result of the spatial inversion using only cross-correlations and three lapse time windows. **(d)** Result of the spatial inversion using only auto-correlations and a single lapse time window. **(e)** Result of the spatial inversion using only auto-correlations and three lapse time windows. **(f)** Result of the spatial inversion from cross-correlations and auto correlations using a single lapse time window. **(g)** Result of the spatial inversion from cross-correlations and auto correlations using a single lapse time window.

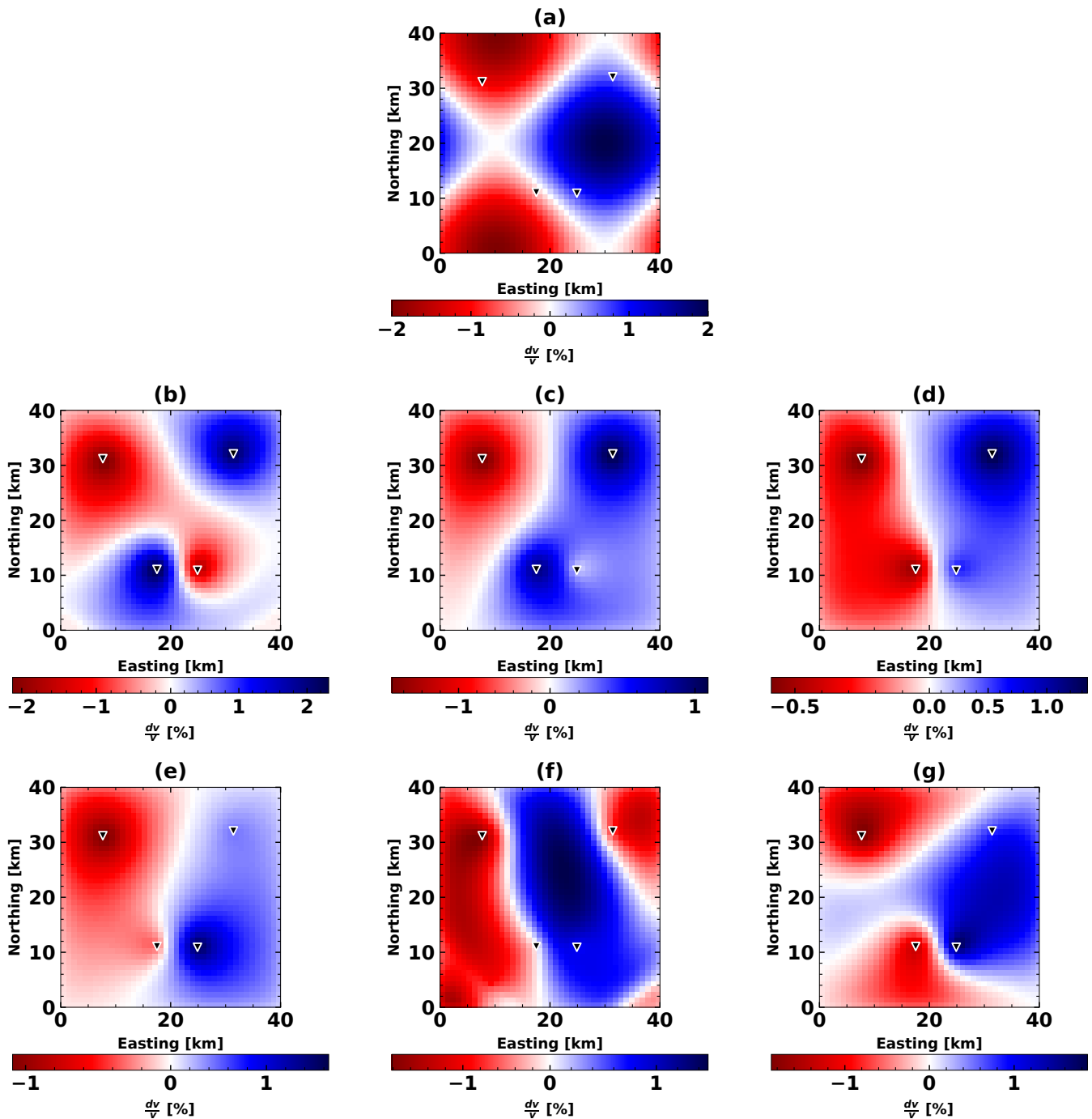


Figure 2 Examples of the spatial inversion using data from four stations, a model variance $\sigma_m = 0.25 \frac{\text{km}}{\text{km}^2}$, and a correlation length $\lambda = 2$ km. **(a)** The synthetic velocity model and station configuration used. **(b)** Result of the spatial inversion using only cross-correlations and a single lapse time window. **(c)** Result of the spatial inversion using only cross-correlations and three lapse time windows. **(d)** Result of the spatial inversion using only auto-correlations and a single lapse time window. **(e)** Result of the spatial inversion using only auto-correlations and three lapse time windows. **(f)** Result of the spatial inversion from cross-correlations and auto correlations using a single lapse time window. **(g)** Result of the spatial inversion from cross-correlations and auto correlations using a single lapse time window.

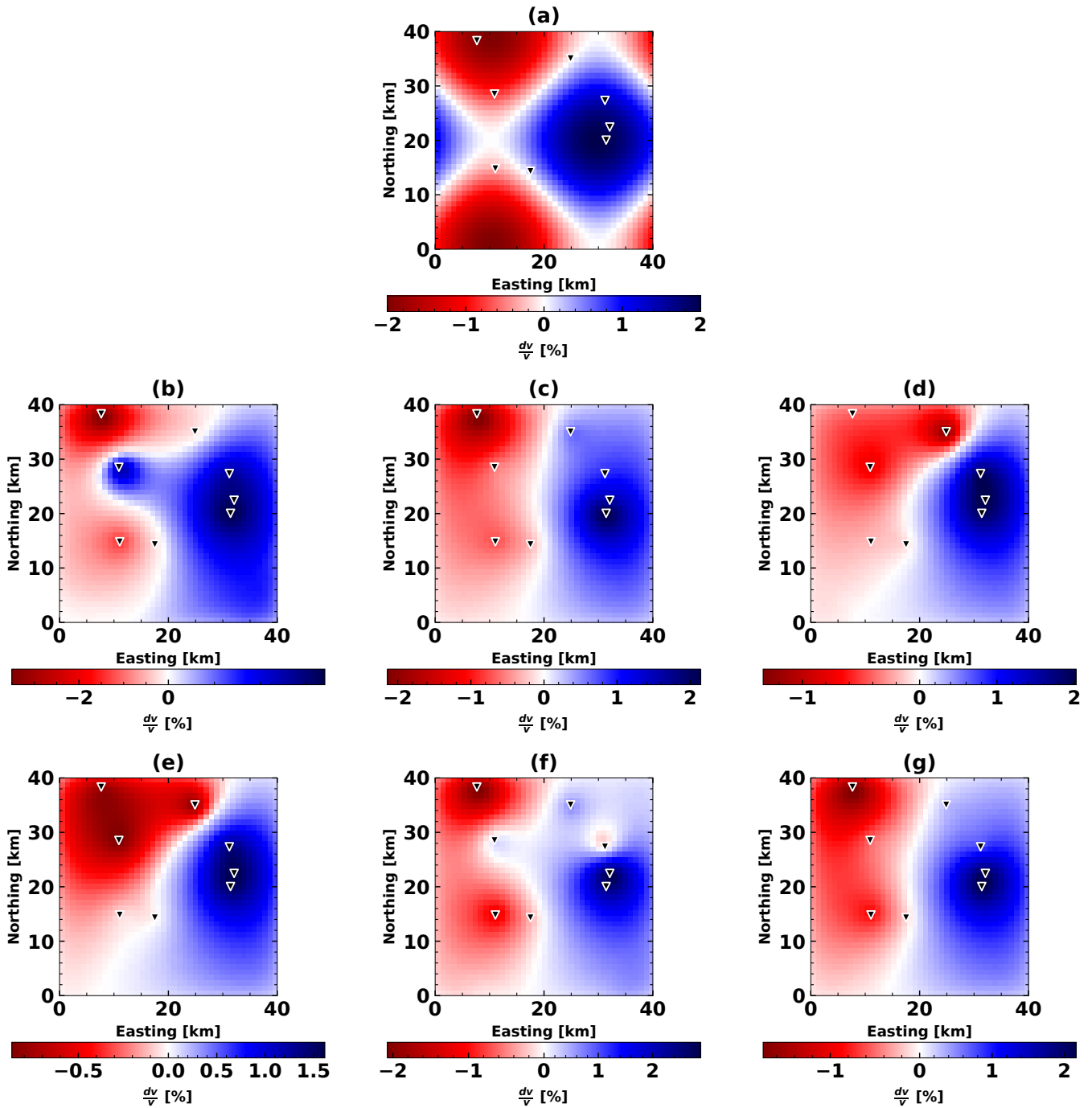


Figure 3 Examples of the spatial inversion using data from eight stations, a model variance $\sigma_m = 0.05 \frac{\text{km}}{\text{km}^2}$, and a correlation length $\lambda = 2$ km. **(a)** The synthetic velocity model and station configuration used. **(b)** Result of the spatial inversion using only cross-correlations and a single lapse time window. **(c)** Result of the spatial inversion using only cross-correlations and three lapse time windows. **(d)** Result of the spatial inversion using only auto-correlations and a single lapse time window. **(e)** Result of the spatial inversion using only auto-correlations and three lapse time windows. **(f)** Result of the spatial inversion from cross-correlations and auto correlations using a single lapse time window. **(g)** Result of the spatial inversion from cross-correlations and auto correlations using a single lapse time window.

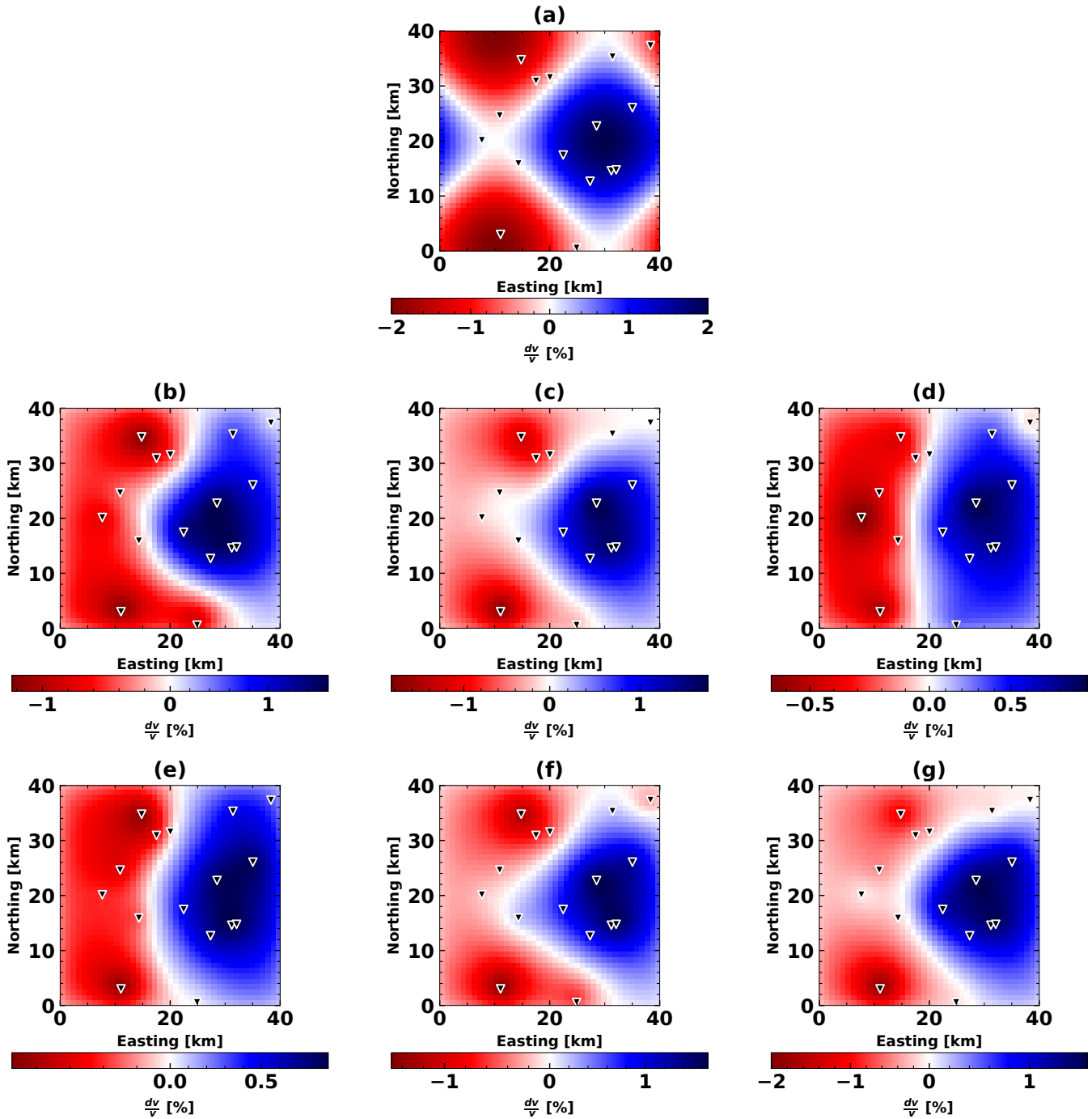


Figure 4 Examples of the spatial inversion using data from 16 stations, a model variance $\sigma_m = 0.02 \frac{\text{km}}{\text{km}^2}$, and a correlation length $\lambda = 2 \text{ km}$. **(a)** The synthetic velocity model and station configuration used. **(b)** Result of the spatial inversion using only cross-correlations and a single lapse time window. **(c)** Result of the spatial inversion using only cross-correlations and three lapse time windows. **(d)** Result of the spatial inversion using only auto-correlations and a single lapse time window. **(e)** Result of the spatial inversion using only auto-correlations and three lapse time windows. **(f)** Result of the spatial inversion from cross-correlations and auto correlations using a single lapse time window. **(g)** Result of the spatial inversion from cross-correlations and auto correlations using a single lapse time window.

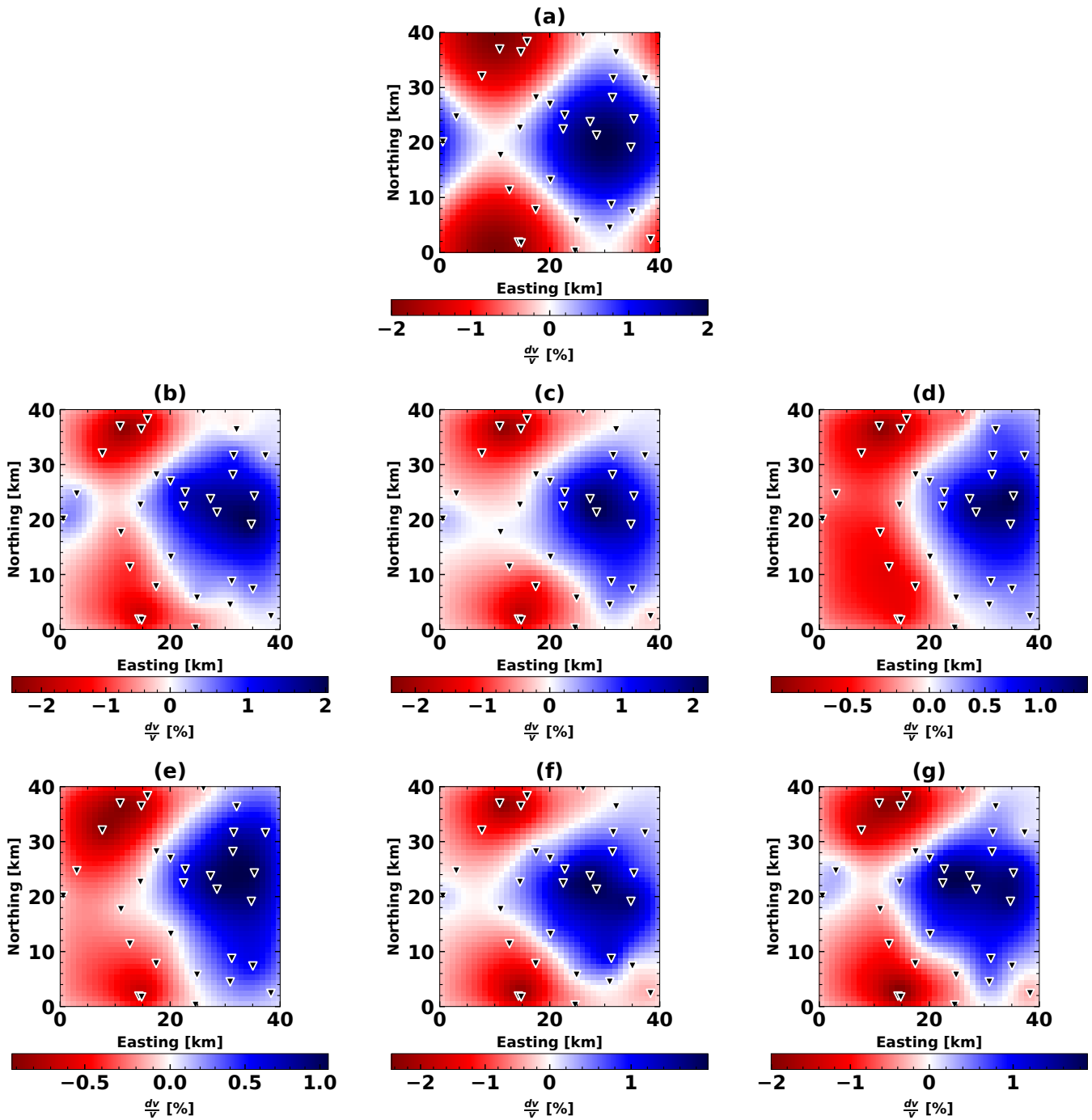


Figure 5 Examples of the spatial inversion using data from 32 stations a model variance $\sigma_m = 0.05 \frac{\text{km}}{\text{km}^2}$ and a correlation length $\lambda = 2$ km. **(a)** The synthetic velocity model and station configuration used. **(b)** Result of the spatial inversion using only cross-correlations and a single lapse time window. **(c)** Result of the spatial inversion using only cross-correlations and three lapse time windows. **(d)** Result of the spatial inversion using only auto-correlations and a single lapse time window. **(e)** Result of the spatial inversion using only auto-correlations and three lapse time windows. **(f)** Result of the spatial inversion from cross-correlations and auto correlations using a single lapse time window. **(g)** Result of the spatial inversion from cross-correlations and auto correlations using a single lapse time window.